# Renormalization of a Finite Range Inverse Cube Potential

D. Odell,[1] A. Deltuva,[2] J. Bonilla,[1] and L. Platter[1,3]

[1]*Department of Physics and Astronomy, University of Tennessee, Knoxville, Tennessee 37996, USA*

[2]*Institute of Theoretical Physics and Astronomy, Vilnius University, Saulėtekio al. 3, LT-10257 Vilnius, Lithuania*

[3]*Physics Division, Oak Ridge National Laboratory, Oak Ridge, Tennessee 37831, USA*

We study the regularization and renormalization of a finite range inverse cube potential in the two- and three-body sectors. Specifically, we compare and contrast three different regulation schemes frequently used to study few-body systems as well as the associated renormalization group (RG) flows. We also calculate bound state and scattering observables over a wide range of cutoffs, demonstrating the sufficiency of a two-body contact interaction to renormalize two- and three-body observables. We supplement these plots with quantified analyses of the observables' residual cutoff dependence.

## I. INTRODUCTION

Effective field theories (EFTs) have become a standard tool in nuclear few-body physics to construct the interactions between the considered degrees of freedom [1, 2]. For example, chiral effective theory is a low-energy expansion of the nucleon-nucleon ($NN$) interaction that employs only nucleons and pions as degrees of freedom and that uses the pion mass $m_\pi$ (or a small momentum) over a large scale $\Lambda$ that can be associated with the lightest degree of freedom not included in the EFT (e.g. the $\rho$-meson). This framework is then used to derive the nuclear Hamiltonian in a systematic low-energy expansion. The resulting potential has been used extensively in few-nucleon studies and ab initio nuclear structure calculations. It was pointed out that the most singular piece of the one-pion exchange (OPE) in the deuteron channel is an inverse cube potential [3, 4]. The renormalization of this leading order (LO) potential has been studied repeatedly in the two- and three-nucleon sector [5–9]. Here, we study the renormalization of the finite range inverse cube potential (FRIC) in the much simpler three-boson system thereby removing the complications due to the

spin-dependent tensor force. In particular, we examine whether the three-body system with pairwise inverse cube interactions requires a three-body counterterm for renormalization, and whether residual cutoff corrections can be used as a reliable tool to build a power counting scheme as suggested in Ref. [10]. We note that there is also interest in atomic physics regarding the inverse cube interaction. However, most attention is focused on the low-energy properties in the *infinite* range limit [11, 12].

Since the residual cutoff dependence to some extent can be influenced by the chosen regularization scheme, we carry out this analysis for various schemes that are currently used by the community. Specifically, we consider a *local* regularization scheme [13] that cuts off the potential in coordinate space at a small distance $R$, a non-local regularization scheme [1] that cuts off the high momenta in the momentum space form of the two-body interaction $V(p, p')$ separately, and a semi-local regularization scheme [14] that applies these strategies separately to the long-range inverse cube part of the interaction and the short-distance regulator.

These different regularization schemes have different advantages for different methods that are used to diagonalize the nuclear Hamiltonian. For example, local interactions are commonly used in quantum Monte Carlo calculations, though progress has been made including nonlocal interactions (e.g. [15, 16]). However, while these have been used extensively in the literature, a detailed comparison of these approaches is missing.

We find that the regularization schemes analyzed can be used to obtain regulator-independent results at large cutoffs. We find however that the regulator dependence of the short-distance counterterm is different for the regulation schemes we apply. In agreement with findings in the three-nucleon sector[6, 9], we find that three-body observables are completely renormalized without the inclusion of an additional three-body counterterm. However, an analysis of the cutoff dependence of three-body observables shows also that observables converge more slowly than expected from previous studies of the three-nucleon sector [9].

In Sec. II, we discuss the regularization schemes as well as the renormalization and calculation of observables. In Sec. III, we present the results obtained for the two- and three-boson system as well as quantitative analyses of the remaining cutoff corrections. We conclude with a summary and an outlook.

## II. THEORY

In the following subsections, we describe the interaction that is used in this work, how it is regulated, and how it is renormalized. We comment also briefly on technical details such as the normalization of states and the calculation of observables through the Schrödinger, Lippmann-Schwinger, and Faddeev equations.

The non-regulated and singular potential $V_S$ that we consider is a FRIC potential of the form

$$V_{\rm S}(r) = -C_3 \frac{e^{-m_\pi r}}{r^3} \ . \tag{1}$$

We choose $m_\pi = 138$ MeV and $C_3 = 0.8$ fm$^2$ such that a deuteron-like state ($B_2 = 2.2$ MeV) exists when we regulate the potential at $\sim 1$ fm. This potential has to be regulated at short distances and observables will depend strongly on the regularization scale as the interaction is too singular [17]. Below we display how a (*smeared out*) short-distance counterterm can be introduced to address this problem.

We perform our calculations in momentum space, and we Fourier transform the interaction $V$ and carry out a partial-wave projection

$$\tilde{V}_l(p,k) \equiv FT\left[V(r)\right] = \frac{2}{\pi}\int_0^\infty dr r^2 j_l(pr) V(r) j_l(kr) \ , \tag{2}$$

where $j_l(z)$ are the spherical Bessel functions of order $l$.

### A. Regulator Formulations

#### 1. Local Regulation

For a local, singular potential, $V_S(r)$, we have implemented three different forms of regulation: local, semi-local, and nonlocal. The locally regulated potential has the form

$$V(r) = \rho(r;R) V_S(r) + g(R)\chi(r;R) \ , \tag{3}$$

where $\rho(r;R)$ is an arbitrary function that minimally fulfills two requirements. First, it must overcome $V_S(r)$ in the $r \to 0$ limit such that the product $\rho(r;R)V_S(r)$ is finite. Second, in the limit of $r \to \infty$, $\rho(r;R)$ must go to one. For the locally regulated case we use

$$\rho(r;R) = \left(1 - e^{-(r/R)^2}\right)^4 \ , \tag{4}$$

where $R$ is the range at which the characteristic behavior of $V_S(r)$ is cut off. The counterterm

$$g(R)\chi(r;R) \ , \tag{5}$$

has two components. The first, $g(R)$ is an $R$-dependent coupling strength. We tune this parameter to match some low-energy, two-body observable such as the two-body binding energy. The second, $\chi(r;R)$, is a contact-like interaction or a *smeared* $\delta$ function such that

$$\lim_{R\to 0}\chi(r;R) \sim \delta(r) \ . \tag{6}$$

For the locally regulated case we use

$$\chi(r;R) = e^{-(r/R)^3} \ . \tag{7}$$

We discuss below that the RG flow of the locally-regulated counterterm strength, $g(R)$, contains multiple branches [18]. To ensure consistency between our results and others', we also implement a semi-local regulation scheme.

### *2. Semi-Local Regulation*

The difference between local regulation and semi-local regulation lies in the definition of the counterterm. In Eq. (3) we defined the counterterm in coordinate space. This counterterm, that regulates the relative distance in the two-body system and thereby the momentum exchange, has multiple solutions (provided the short-distance cutoff is small enough) for which the two-body binding energy $B_2$ is reproduced.

If we instead define the counterterm in momentum space as

$$g(R)\tilde{\chi}(p;R)\tilde{\chi}(k;R) \ , \tag{8}$$

such that, by itself, only permits one state, we obtain a unique RG flow. The full potential in momentum space is then

$$\tilde{V}(p,k) = FT\left[\rho(r;R)V_S(r)\right] + g(R)\tilde{\chi}(p;R)\tilde{\chi}(k;R) \ , \tag{9}$$

where $FT$ represents the Fourier transform and partial-wave projection shown in Eq. (2).

For the semi-locally regulated case, similar to [14], we use

$$\rho(r;R) = \left[1 - e^{-(r/R)^2}\right]^4 \ , \tag{10}$$

and

$$\tilde{\chi}(p;R) = e^{-(pR/2)^2} = e^{-(p/\Lambda)^2} \ , \tag{11}$$

where $\Lambda \equiv 2/R$. For a brief discussion on the different $\rho(r;R)$ functions used for the locally and semi-locally regulated cases, see Appendix A.

#### *3. Nonlocal Regulation*

For the fully nonlocal interaction, we take the semi-local interaction Eq. (9), including the forms of $\rho(r;R)$ and $\tilde{\chi}(p;R)$, and modify the first term as follows

$$\tilde{V}(p,k) = \tilde{\chi}(p;R) FT\left[\rho(r;R_<)V_S(r)\right]\tilde{\chi}(k;R) + g(R)\tilde{\chi}(p;R)\tilde{\chi}(k;R) \ . \tag{12}$$

The momentum-space regulators multiplying the first term suppress the diagonal matrix elements where the incoming and outgoing momenta are large but similar, removing some sensitivity to the choice of $\rho(r;R)$ that we discuss in A. The short-distance cutoff used before we take the Fourier transform, $R_<$, is chosen to be much less than $R$. This allows us to ensure that the resulting cutoff dependence in the observables is attributable to the regulator function, $\tilde{\chi}(p;R)$, rather than the Fourier transform.

### B. Two-Body Bound States

We calculate two-body binding energies by solving the Schrödinger equation

$$(\hat{H}_0 + \hat{V})\,|\psi\rangle = E\,|\psi\rangle \ , \tag{13}$$

in coordinate and momentum space. In coordinate space, we tune the counterterm such that for a desired value $E$, the radial equation

$$-\frac{1}{m}\frac{d^2u}{dr^2} + V(r)u(r) = E\,u(r) \ , \tag{14}$$

is solved where $u(r) \equiv rR_0(r)$. We have dismissed the centrifugal term as only s-waves are considered. In momentum space, we rearrange Eq. (13) such that we have

$$\hat{G}_0(E)\hat{V}\,|\psi\rangle = |\psi\rangle \ , \tag{15}$$

where $G_0(z) \equiv 1/(z - \hat{H}_0)$. After discretization with the basis states $|p_i\rangle$, Eq. (15) becomes an eigenvalue problem that is easily solved by finding the energies that fulfill

$$\det\left[\hat{1} - K_{ij}(E)\right] = 0 \ , \tag{16}$$

where $K_{ij}(E) = \langle p_i|\hat{G}_0(E)\hat{V}|p_j\rangle$ and we tune the counterterm such that the requirement Eq. (16) is satisfied.

### C. Lippmann-Schwinger Equation

To obtain two-body phase shifts, we solve numerically the Lippmann-Schwinger Equation for the two-body $t$-matrix

$$\hat{t} = \hat{V} + \hat{V}\hat{G}_0\hat{t} \ . \tag{17}$$

In the partial-wave projected momentum basis, considering bosons interacting in $s$-waves only, we have

$$\begin{aligned} \langle p\,|\hat{t}|p'\rangle &= \langle p\,|\hat{V}|p'\rangle + \langle p\,|\hat{V}\,\hat{G}_0(E+i\epsilon)\,t|p'\rangle \ , \\ t(p,p';E) &= \tilde{V}(p,p') + \int_0^\infty dq\, q^2\, \frac{\tilde{V}(p,q)\,t(q,p';E)}{E + i\epsilon - q^2/m} \end{aligned} \tag{18}$$

where $m$ is the nucleon mass and $\epsilon \to +0$. From the on-shell matrix element $t(p,p;E = p^2/m)$ we extract the phase shift via

$$t(p,p;E = p^2/m) = -\frac{2}{m\pi}\frac{1}{p\cot\delta - ip} \ . \tag{19}$$

The scattering length is defined by the effective range expansion

$$p\cot\delta \approx= -\frac{1}{a} + \frac{r_s}{2}p^2 \ , \tag{20}$$

which allows us to calculate it exactly from the on-shell $t$-matrix amplitude at $p = 0$.

$$a = \frac{m\pi}{2}t(0,0;0) \ . \tag{21}$$

### D. Three-Body Bound States

To calculate three-body binding energies, we start with the equation for a single Faddeev component of a system containing three identical particles

$$|\psi\rangle = \hat{G}_0(E)\hat{t}\hat{P}\,|\psi\rangle \ , \tag{22}$$

where

$$\hat{P} = \hat{P}_{12}\hat{P}_{23} + \hat{P}_{13}\hat{P}_{23} \ , \tag{23}$$

is the permutation operator with $\hat{P}_{ij}$ interchanging particles $i$ and $j$ [19]. After projecting onto the partial-wave, momentum basis for three identical bosons described by two Jacobi momenta $p$ (the relative momentum between particles 1 and 2) and $q$ (the relative momentum between particle 3 and the center of mass of the 1–2 subsystem), we discretize the equation and solve for the bound state energy $E$ using the same techniques as in the two-body case, as long as $E$ remains below the deepest state in the two-body spectrum. However, this limitation is in conflict with our goal of studying the cutoff dependence of two- and three-body observables. As we go to higher momentum-space cutoffs (smaller $R$ values), spurious bound states enter the two-body spectrum. Three-body states quickly become resonances in this regime, bounded above and below by two-body bound states. There are two ways that we deal with this.

The first method follows [6] and is repeated here. It involves *removing* the spurious two-body state from the spectrum by transforming the potential

$$\hat{V} \to \hat{V} + |\phi\rangle \, \lambda \, \langle\phi| \ , \tag{24}$$

which takes the eigenvalue of the state $\phi$ and modifies it by an amount $\lambda$. Using this transformed potential in the Lippmann-Schwinger equation and taking the limit of $\lambda \to \infty$ (removing the state from the spectrum), we have

$$\lim_{\lambda\to\infty} \hat{t}(\lambda) = \hat{t} - |\eta\rangle \, \frac{1}{\langle\phi|\hat{G}_0|\eta\rangle} \, \langle\eta| \ , \tag{25}$$

as our modified $t$-matrix where

$$|\eta\rangle = |\phi\rangle + \hat{t}\hat{G}_0 \, |\phi\rangle \ . \tag{26}$$

This only requires that we have the wave function $\langle p|\phi\rangle$ to calculate the modified $t$-matrix where that state no longer contributes a pole. In practical calculations using a large, finite $\lambda$ value in (24) is sufficient. If there are several spurious two-body states, the procedure is repeated for each of them.

The second method we employ to study the cutoff dependence of three-body resonances is to look for the resonances in the three-body phase shifts.

### E. Three-Body Phase Shifts

In the cutoff regime where spurious two-body bound states exist, we can scatter a third particle off the spurious deep two-body state and scan the phase shifts in the energy range between the two-body states for a resonance. To do this, we calculate the three-body $T$-matrix using [20]

$$\hat{T} = \hat{t}\hat{P} + \hat{t}\hat{G}_0\hat{P}\hat{T} \ , \tag{27}$$

which relates to the elastic scattering operator $\hat{U}$ by

$$\hat{U} = \hat{P}\hat{G}_0^{-1} + \hat{P}\hat{T} \ . \tag{28}$$

In the partial-wave-projected, momentum basis, considering bosons interacting only via $s$-waves, we have

$$\begin{aligned} \langle pq|\hat{T}|\phi\rangle = \langle pq|\hat{t}\hat{P}|\phi\rangle + \\ \int_0^\infty dq'(q')^2 \int_{-1}^{1} dx \, \frac{t(p,\pi_1, E-3q^2/4m)\, G(q,q',x)}{E+i\epsilon - q^2/m - (q')^2/m - qq'x/m} \, \langle \pi_2 q'|\hat{T}|\phi\rangle \ , \end{aligned} \tag{29}$$

where the incoming state $|\phi\rangle = |\varphi k\rangle$ contains the wave function $\varphi(p)$ of the two-body bound state and the relative momentum $k$ between the third particle and the center of mass of the two-body subsystem, $G(q,q',x)$ is a geometrical factor introduced by the permutation operator, $\pi_1 = \sqrt{q^2/4 + (q')^2 + qq'x}$, and $\pi_2 = \sqrt{q^2 + (q')^2/4 + qq'x}$.

The elastic scattering amplitude $M$ is related to the $U$ operator by

$$M = -\frac{2m\pi}{3} \langle \phi|\hat{U}|\phi\rangle \ , \tag{30}$$

and the phase shift by

$$M = \frac{1}{k\cot\delta - ik} \ . \tag{31}$$

In the three-body sector, we have a similar effective range expansion

$$k\cot\delta \approx -\frac{1}{a_{AD}} + \frac{r_{s,AD}}{2}k^2 \ , \tag{32}$$

which defines the atom-dimer scattering length $a_{AD}$ and atom-dimer effective range $r_{s,AD}$. We also study the inelasticity parameter given in terms of the $S$-matrix by

$$\eta = e^{-2\delta_i} \ , \tag{33}$$

where the phase shift is complex and the usual decomposition

$$\delta = \delta_r + i\delta_i \ , \tag{34}$$

is taken.

### F. Quantitative Uncertainty Analysis

To analyze the uncertainties induced by short-distance physics of our regularization procedure, we study in this section the regulator dependence of observables. Similar to the analysis done by Song *et al.* [9], our uncertainty analysis is based on a simple power series expansion of observables quantities $\mathcal{O}$ of the form

$$\mathcal{O}(\Lambda) \approx \mathcal{O}_\infty \left[1 + \sum_i^\infty c_i \left(\frac{q}{\Lambda}\right)^i\right] \ , \tag{35}$$

where $q$ is associated with the low-momentum scale relevant to the calculation; however, $i$ is *not* assumed to be an integer. For the purposes of this project, we truncate the summation over $i$ after the first term $i = n$, leaving

$$\mathcal{O}(\Lambda) \approx \mathcal{O}_\infty \left[1 + c_n \left(\frac{q}{\Lambda}\right)^n\right] \ , \tag{36}$$

We seek to establish the value of $n$. In Ref. [9], $n$ was found by fitting the first few terms in the above expansion with integer $n$ to the cutoff dependence of observables. Here, we study the cutoff dependence at very large cutoffs, focus on the dominant term in the expansion, and fit $n$ itself to data and allow for non-integer values.

To extract the power of the leading cutoff correction, we examine both the $\Lambda$ and the $q$ dependence. The first approach we take to investigate the $\Lambda$ dependence is to calculate observable $\mathcal{O}$ over a range of $\Lambda$ values, and fit the results to Eq. (36) for a range of $n$ values. For each $n$, we evaluate a penalty function that we define as

$$p_n = \sum_i \left(\frac{\mathcal{O}_{calc}(\Lambda_i) - \mathcal{O}_{fit}(\Lambda_i)}{\mathcal{O}_{calc}(\Lambda_i)}\right)^2 \ , \tag{37}$$

where $\mathcal{O}_{calc}(\Lambda)$ is the observable calculated for a specific value of $\Lambda$ and $\mathcal{O}_{fit}(\Lambda)$ is the value of the observable as it is "reproduced" by Eq. (36) and the fit parameters $\mathcal{O}_\infty$ and $c_n$. Once we have $p_n$ for a range of $n$ values, we search for a minimum $p_n$ where $n$ is optimal.

Griesshammer has shown [10] that the $q$ dependence of observables provides a necessary though insufficient window into the order of cutoff-dependent corrections. To isolate the $q$ dependence, we have to restrict the observables we study to those whose $q$ dependence is well understood. Doing so allows us to calculate the observable at two different cutoffs and study the relative difference

$$1 - \frac{\mathcal{O}(\Lambda_1)}{\mathcal{O}(\Lambda_2)} \approx q^n c_n \left[\frac{1}{\Lambda_2^n} - \frac{1}{\Lambda_1^n}\right] \ . \tag{38}$$

Taking the logarithm, we get

$$\ln\left[1-\frac{\mathcal{O}(\Lambda_1)}{\mathcal{O}(\Lambda_2)}\right]=n\ln q+b\ , \tag{39}$$

where $n$ and $b$ are the slope and intercept that we fit, respectively.

## III. RESULTS

### A. Renormalization Group Flow

The first thing we compare between the regulation schemes is the RG flow. We choose to fix the shallowest two-body state at $B_2 = 2.2$ MeV. Figure 1 shows the stark difference between the RG flow found using a local counterterm and the RG flows found with nonlocal counterterms. The main difference is the issue of uniqueness. For the locally regulated potential, as pointed out by [18], $g(R)$ has multiple solutions that give a two-body bound state at the desired binding energy. There is one branch where there exists one state in the two-body system. Each branch below that branch contains successively one additional state. The RG flow shown for the locally regulated interaction connects four of those branches, "hopping" downward when it is easier to add an additional state than to continue to maintain the shallowness of the fixed state. Only two of the "hops" are visible in the plot due to the scale and the relative difference between the magnitudes of $g$ between the different branches. Note also the difference in the units of the upper and lowers plots if Fig. 1. There is a factor of $R^3$ that comes from the Fourier transform and partial-wave projection of $\chi(r;R)$.

The other two functions shown in the lower plot of Fig. 1 are qualitatively very similar. They correspond to the semi-local and nonlocal regulation schemes. While the same $\rho(r;R)$ is used in both, the prescription is somewhat different as one can see from Eq. (9) and Eq. (12). The semi-local regulation scheme brings in spurious bound states faster than the nonlocal regulation scheme, but as mentioned before, nonlocal regulation cuts off the potential at large incoming and outgoing momenta, suppressing high-momentum contributions. Still, they are very similar interactions, thus they provide very similar RG flows.

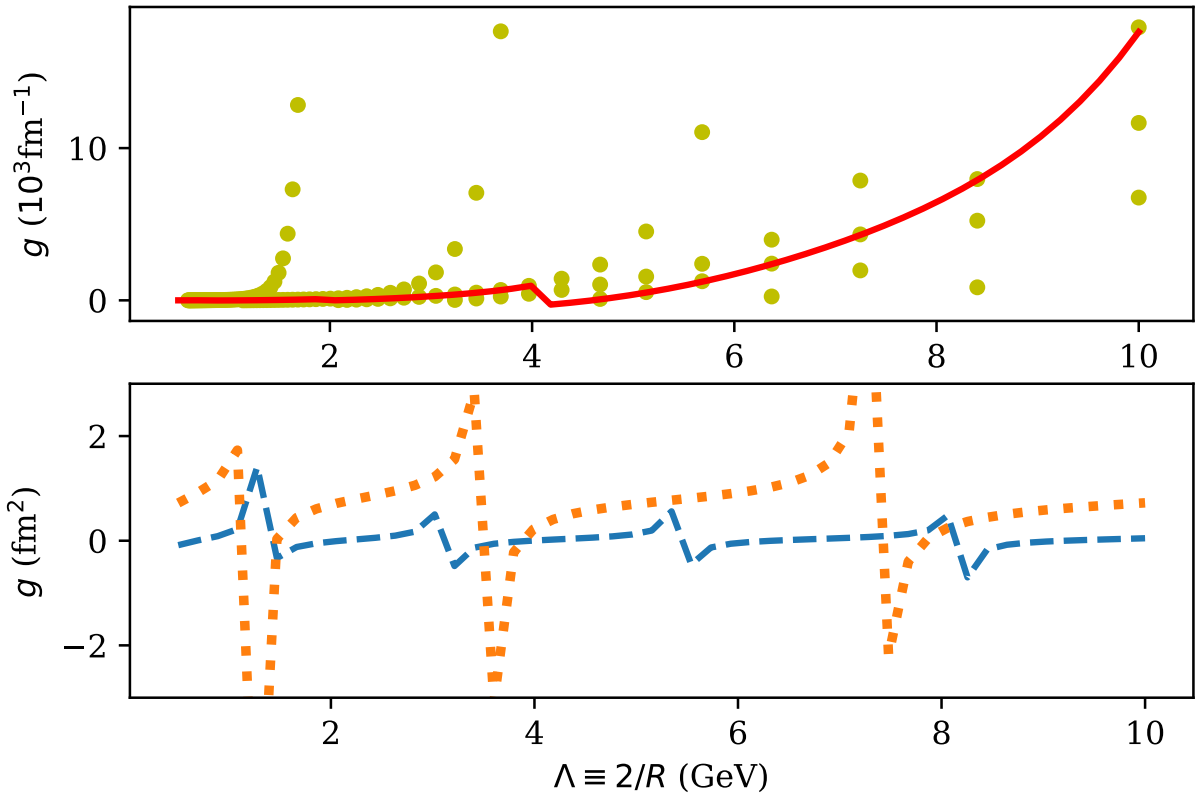


FIG. 1. RG flows of the counterterm coupling $g$. The yellow circles in the upper plot represent $g(R)$ values calculated with a local regulator and local counterterm. The red, solid line in the upper plot are the $g(R)$ values used to calculate the phase shifts in Fig. 2. The blue, dashed line in the lower plot corresponds to the semi-locally regulated interaction. The orange, dashed line corresponds to the nonlocally regulated interaction.

### B. Two-Body Scattering

As the different regulation schemes are tuned to reproduce the same shallow state at $B_2 = 2.2$ MeV, we expect that differences in low-energy scattering observables are highly suppressed when large cutoffs are employed. We calculate the phase shifts using all three regulation schemes and show the results in Fig. 2. The left plot contains the phase shifts of an non-renormalized, nonlocally regulated potential with $g(R) = 0$, demonstrating the strong cutoff dependence of low-energy observables and the need for a counterterm. The most important feature of the right plot is the agreement between the different regulation schemes. It is also worth mentioning the "turning point" $\Lambda$ value at which phase shifts clearly begin

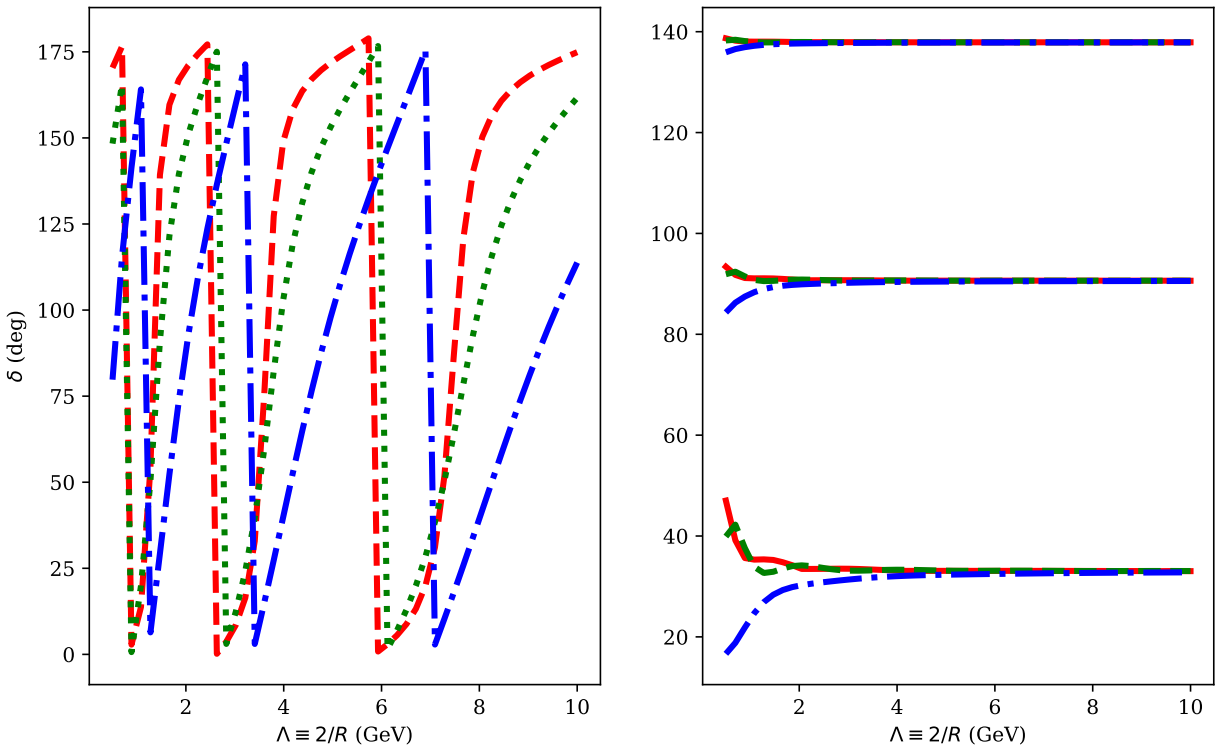


FIG. 2. [Left] Cutoff dependence of the s-wave phase shifts at $E = 1$ (red, dashed), 10 (green, dotted), and 100 MeV (blue, dot-dashed) calculated via a nonlocally regulated potential without a counterterm. [Right] Cutoff dependence of the s-wave phase shifts at (from top to bottom) $E = 1$, 10, and 100 MeV in the center-of-mass frame. The solid, red lines are the phase shifts calculated from a locally regulated potential. The green, dashed lines are the phase shifts at the same energies calculated with a semi-locally regulated interaction. The blue, dot-dashed lines are the phase shifts using a nonlocally regulated interaction. All three schemes include a contact-like counterterm.

to flatten out. At low energies, the point is near 2 GeV. As the scattering energy increases that point increases as well. Importantly, this behavior agrees with studies of the OPE potential [6, 9] where similar convergence behavior is found across a range of partial-wave channels. Our $C_3$ value is chosen to mimic the OPE in the bosonic sector such that we can expect similar renormalization behavior. Observing this similarity is consistent with the known result that the one-pion-exchange potential goes like an inverse cube potential at short distances (high cutoffs) [3, 4].

It is clear from Fig. 2 that a two-body contact interaction is sufficient to renormalize the two-body phase shifts. The corresponding result for the two-body scattering length is shown

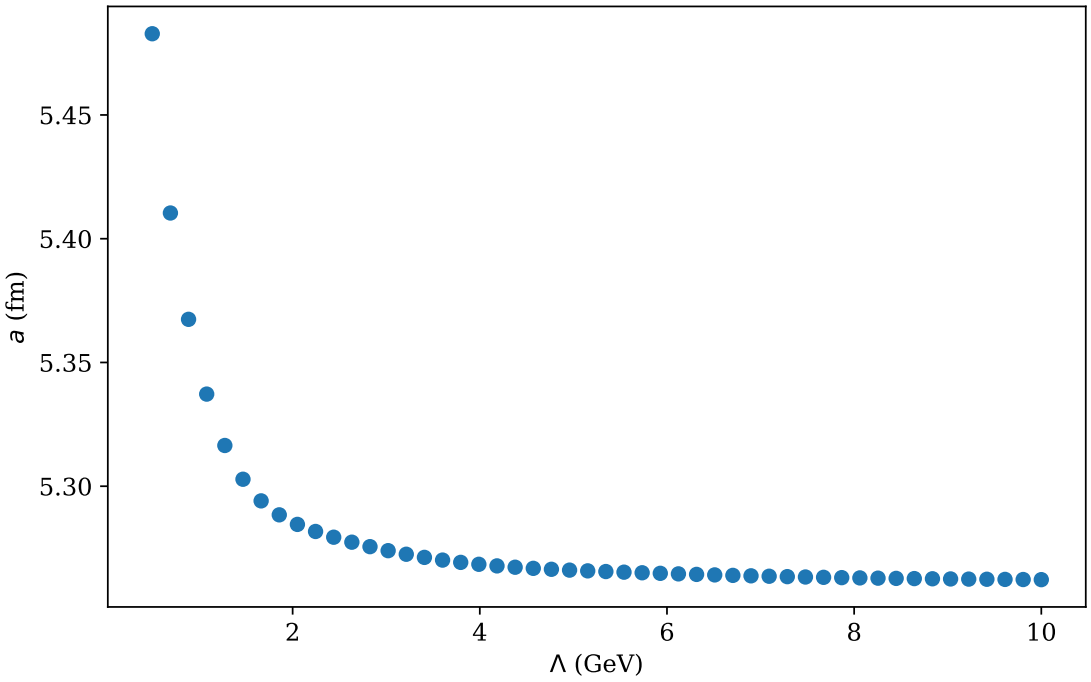


FIG. 3. The scattering length is shown as a function of the high-momentum (short-distance) cutoff. The blue circles are the numerical results.

in Fig. 3.

One of the advertised, key advantages of EFT is quantifiable uncertainty which in turn requires a power counting that orders contributions in the Hamiltonian according to their importance. These uncertainties have usually two sources: (i) the truncation of the low-energy expansion and (ii) uncertainties that are introduced when low-energy counterterms are fitted to data. Here we focus on the first source of uncertainties and some information on this truncation error is contained in the convergence behavior of observables as the short-distance cutoff is increased. To study this problem, we first chose a range of cutoffs over which to fit the scattering length to Eq. (36). However, as the window of cutoffs over which the fit was carried out was narrowed to include only the highest values of $\Lambda$, the resulting $n$ was found to be unstable. As a result, we plotted $\Lambda(da/d\Lambda)$, shown in Fig. 4. The solid, red line in the left-hand plot of Fig. 4 is the expected $\Lambda(da/d\Lambda)$ dependence based on a fit to Eq. (36) with $n = 1.5$. Clearly, there is behavior in the cutoff dependence of the scattering length that is not captured by the simple form assumed in Eq. (36).

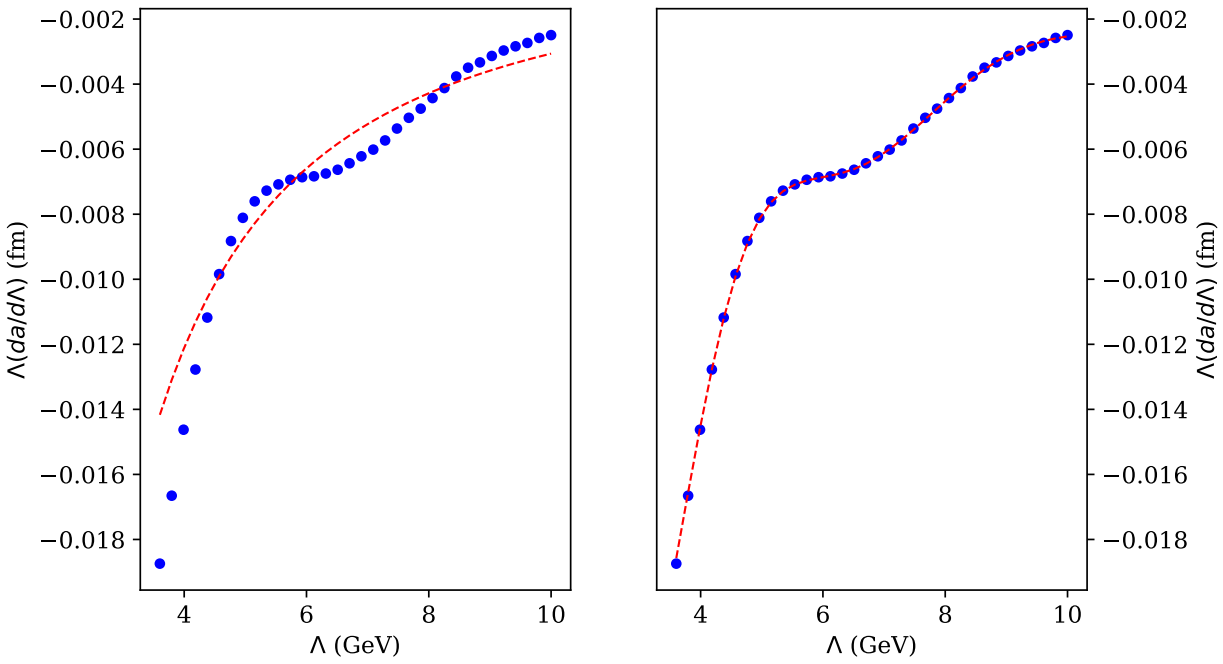


FIG. 4. [Left] RG analysis of the two-body scattering length as a function of the cutoff. Blue circles represent the data. The red, dashed line represents a fit to Eq. (36) with $n = 1.5$. [Right] The blue circles represent the same data as the left-hand plot. The red, dashed line represents a fit to Eq. (40) with $n_{\rm min} = 1.7$.

Empirically, we model the residual cutoff dependence by

$$\Lambda \frac{da}{d\Lambda} \approx \frac{1}{\Lambda^n} \left[ A + B \cos\left( h\Lambda^{1/3} + f \right) \right] \ , \tag{40}$$

where $A, B, h$ and $f$ are treated as fit parameters. We choose a range of $n$ values over which we carry out the fit and evaluate the quality of the fit with Eq. (37) at each value. The right-hand plot of Fig. 4 shows $\Lambda(da/d\Lambda)$ in blue circles with $n_{\rm min} = 1.7$. The red, dashed line in the left-hand plot of Fig. 4 represents Eq. (40) with the fit parameters found when using $n_{min}$. The agreement between the data and the empirical formula is excellent.

We expect that all low-energy, two-body observables come with similar cutoff dependence. In keeping with our study of the cutoff dependence of the scattering length, we applied the same analysis to the phase shifts and cross sections. In Fig. 5 we plot the results. In both cases, the calculation was performed at a relative, center-of-mass momentum of 106 MeV. The analyses produced minima of the penalty functions (Eq. (37)) near $n_{\rm min} = 1.7$. Similar analyses performed at different energies produced similar results. The only trend worth

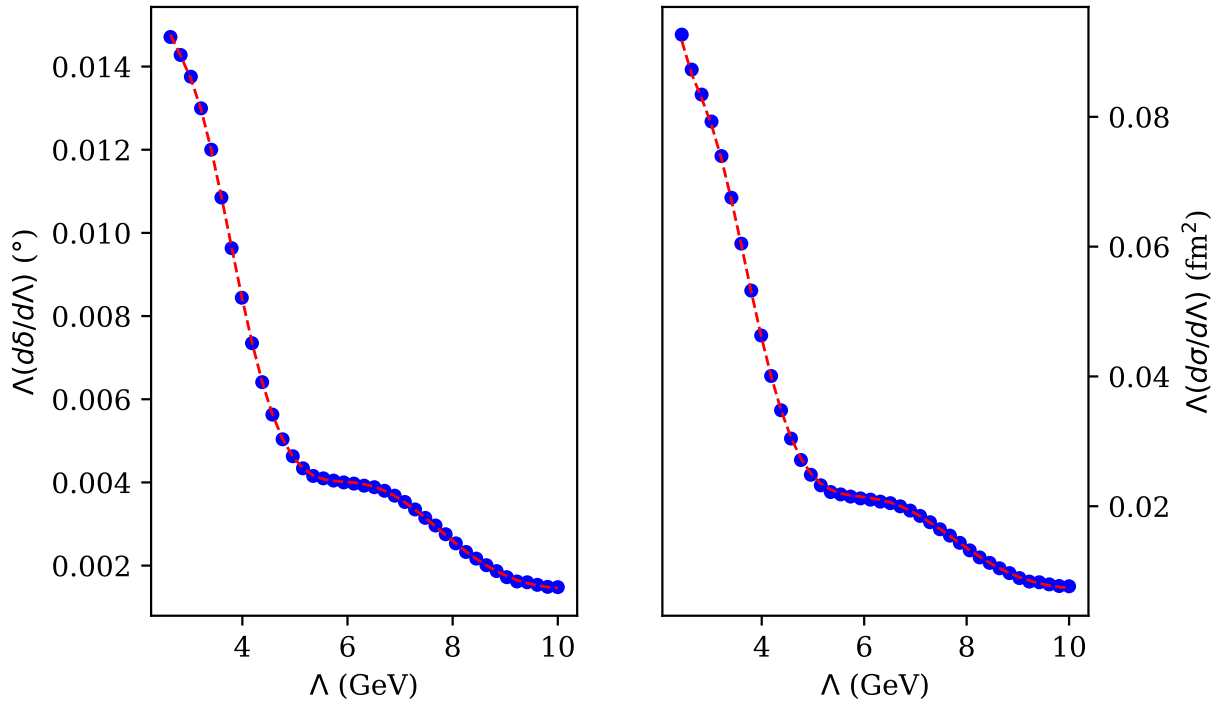


FIG. 5. [Left] RG analysis of the phase shift at a center-of-mass momentum of 106 MeV as a function of the cube root of the cutoff. Blue circles represent the data. The red, dashed line represents a fit to Eq. (40) with $n_{\min} \approx 1.7$. [Right] The same analysis of the cross section at a center-of-mass momentum of 106 MeV as a function of the cube root of the cutoff. The legend is the same as in the left-hand plot.

mentioning is the slight decrease of $n_{\min}$ to approximately 1.5 as the scattering energy increases. Overall, the agreement between the data and Eq. (40) found for the scattering length is found for the phase shift and cross section as well. The $n_{\min}$ values are collected in Table I.

Interestingly, the $h$ values vary by less than a few percent around 1.5 MeV$^{-1/3}$ between the observables. This fairly constant oscillation frequency matches up with the frequency of new bound states in the RG flow. As shown below, this correspondence carries over to the three-body sector as well.

The order of corrections is independent of the method used to obtain it. In that spirit, we apply in addition to our modified power series expansion the method proposed by Griesshammer [10]. Fig. 6 shows the comparison of the phase shifts at $\Lambda = 3408$ and 6704 MeV. By Eq. (39), we expect the behavior to be linear. In fact, we are able to extract a reliable slope

of $n = 1.5$ by fitting the data to Eq. 39. Unfortunately, we found that other observables such as the cross section and $k \cot \delta$ provide unreliable results. Specifically, zeros and unpredictable crossings precluded the extraction of linear behavior. Selecting the phase shifts as the quantities of interest follows naturally from these unfortunate conditions as discussed by Griesshammer [10].

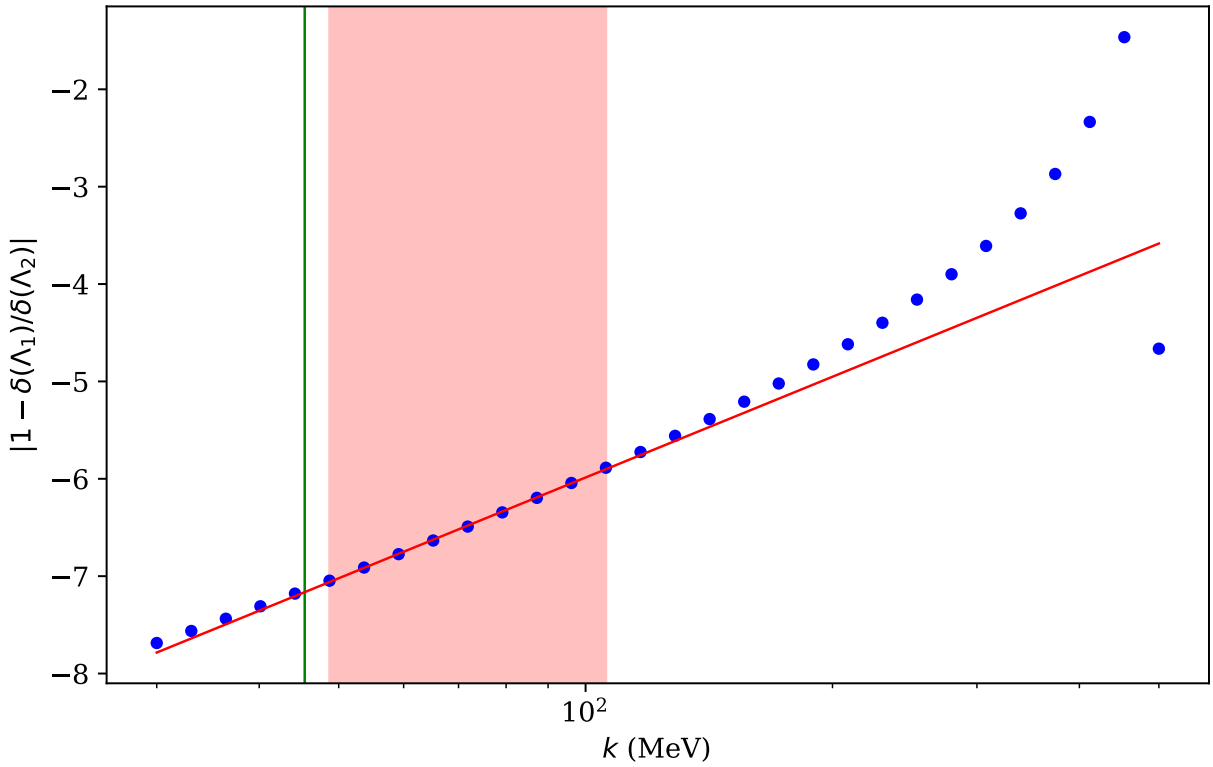


FIG. 6. Residual cutoff corrections to the two-body phase shifts as a function of the relative momentum. The blue circles represent the numerical calculation. The red line represents a fit to Eq. (39), resulting in $n = 1.5$. The pink, shaded region represents the range of $k$ over which the fit was performed. The vertical, green line is the binding momentum $\gamma$.

### C. Three-Body Scattering

The first observable in the three-body sector that we study is the atom-dimer scattering length. Figure 7 shows the convergence of $a_{\mathrm{AD}}$ with respect to the momentum cutoff $\Lambda$, clearly demonstrating that a two-body contact term is sufficient to renormalize three-body observables.

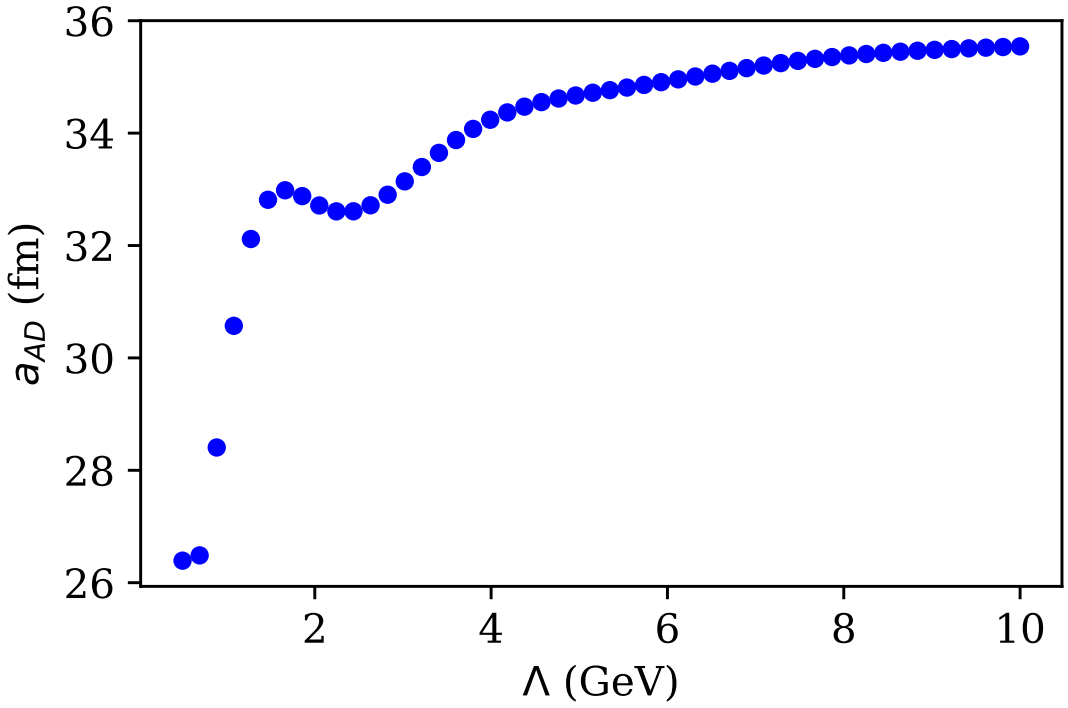


FIG. 7. The cutoff dependence of the atom-dimer scattering length.

Again, we apply the analysis based on Eq. (40) to the atom-dimer scattering length. The results are shown in Fig. 8. As in the two-body sector, Eq. (40) is able to accurately describe the oscillatory convergence behavior occuring on top of the typically expected Λ-dependence. The fit was performed over a range of cutoffs — from $\Lambda_{\text{lower}} = 3.1$ GeV to $\Lambda_{\text{upper}} = 8.1$ GeV. For the atom-dimer scattering length, the best fit to Eq. (40) occurs at $n_{\text{min}} = 1.3$. Because this analysis involves the derivative of the observable with respect to Λ and three-body observables are particularly difficult to obtain to arbitrary accuracy, we are often forced to constrain our fit window. The atom-dimer scattering length, as well as the other three-body observables presented below, are selected because they provide stable results over a significant range of cutoffs.

In addition to the atom-dimer scattering length, we also conduct analyses of three-body phase shifts and inelasticities at center-of-mass, kinetic energies of 10, 50, and 100 MeV. The results are shown in Fig. 9. The $n_{\text{min}}$ values, ranging from 1.1 to 1.3, used to plot the solid, red lines corresponding to Eq. 40 are tabulated in Table I. The bounds of the cutoff range are included as well to assure the reader that the behavior represents a significant and

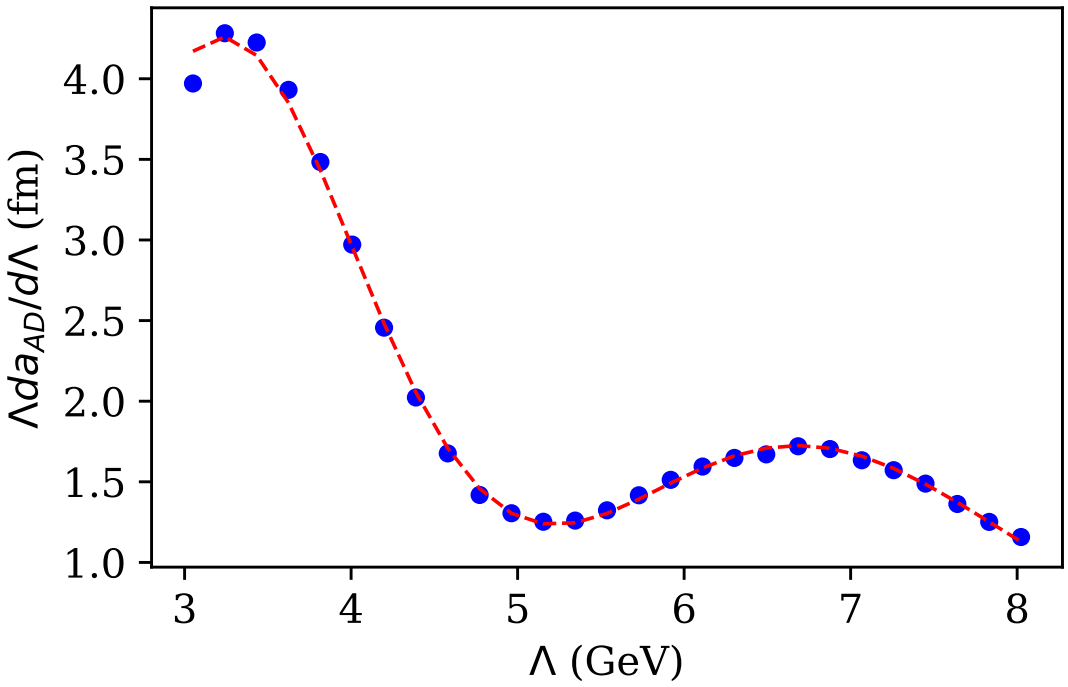


FIG. 8. $\Lambda(da_{AD}/d\Lambda)$ as a function of the momentum-space cutoff. The blue circles are the calculation. The solid, red line is the fit to Eq. (40) with $n_{\min} = 1.3$.

relevant portion of the cutoff dependence.

### D. Three-Body Bound States

One of the main goals of these efforts has been to examine the sufficiency of a two-body counterterm to renormalize three-body observables. In Fig. 10 we plot the cutoff dependence of the three-body binding energies associated with two three-body states that appear in the system defined by the nonlocally regulated interaction Eq. (12). The results shown come from the solution of Eq. (22), though equivalent results were found by calculating the three-body phase shifts defined by Eq. (31) and scanning for resonances. The ground state and excited state binding energies at $\Lambda = 10$ GeV are -18.086 MeV and -2.2379 MeV, respectively. The primary feature of Fig. 10 is the convergence of the binding energies in the infinite $\Lambda$ limit. At $\approx 2$ GeV, the binding energies (or rather, the resonant energies) begin to flatten out, just as in the two-body phase shifts.

Unfortunately, small inaccuracies in the three-body binding energies left only small win-

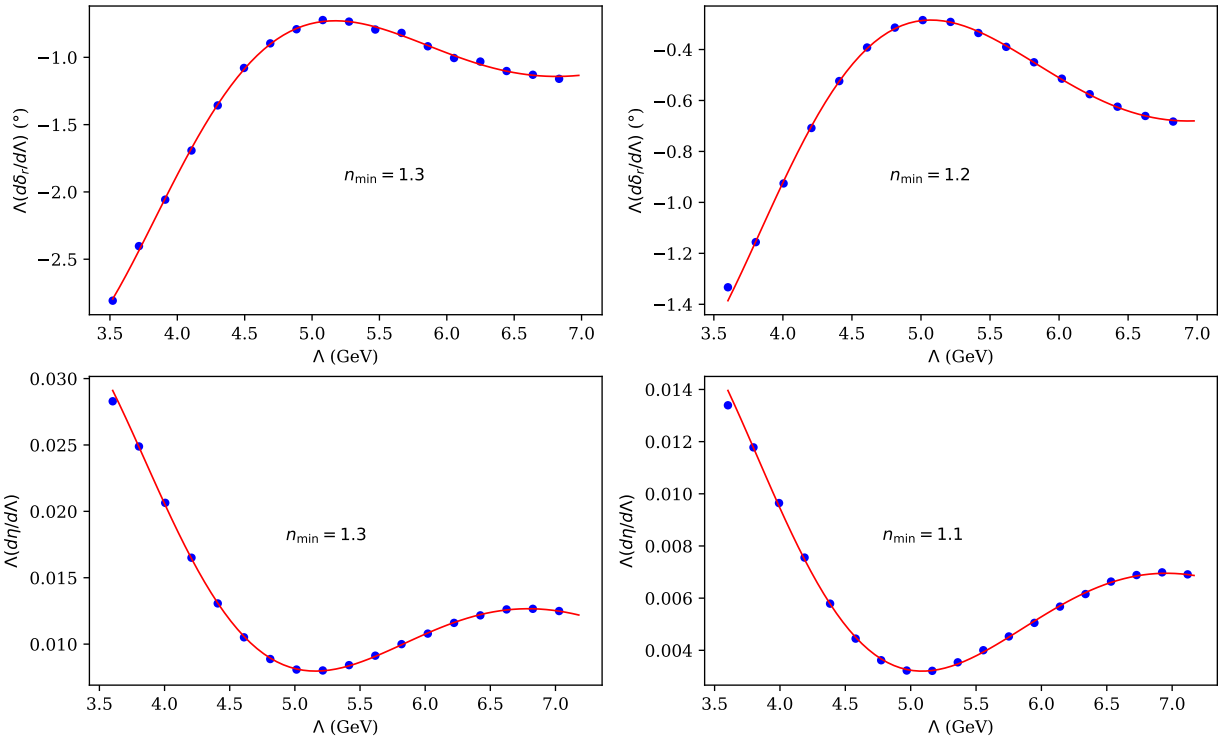


FIG. 9. [Upper Left] Eq. 40-based analysis of the 2+1 phase shift at $E = 10$ MeV. The blue circles are the calculation. The solid, red line is the fit to Eq. 40. [Upper Right] Same analysis and legend applied to the 2+1 phase shift at $E = 50$ MeV. [Lower Left] Inelasticity at $E = 50$ MeV. [Lower Right] Inelasticity at $E = 100$ MeV.

dows of cutoffs over which a fit to Eq. (40) could be performed when all four fit parameters were treated as such. Using the values of $h$ and $f$ from the fit of the atom-dimer scattering length to Eq. (40), we fit only $A$ and $B$ for the ground state binding energy and show the results in Fig. 11. An $n_{\min}$ value of 1.4 is found to minimize the penalty function, and the form of Eq. (40) is further validated.

Throughout all of the three-body observables, we see a consistency among the $h$ values. Notably, it is enforced manually for the three-body ground state. They range from 1.4 to 1.5 MeV$^{-1/3}$ which is also consistent with the $h$ values found by fitting the two-body observables. This consistency between the two- and three-body sectors can be seen in Table I which establishes the pervasive nature of these oscillations.

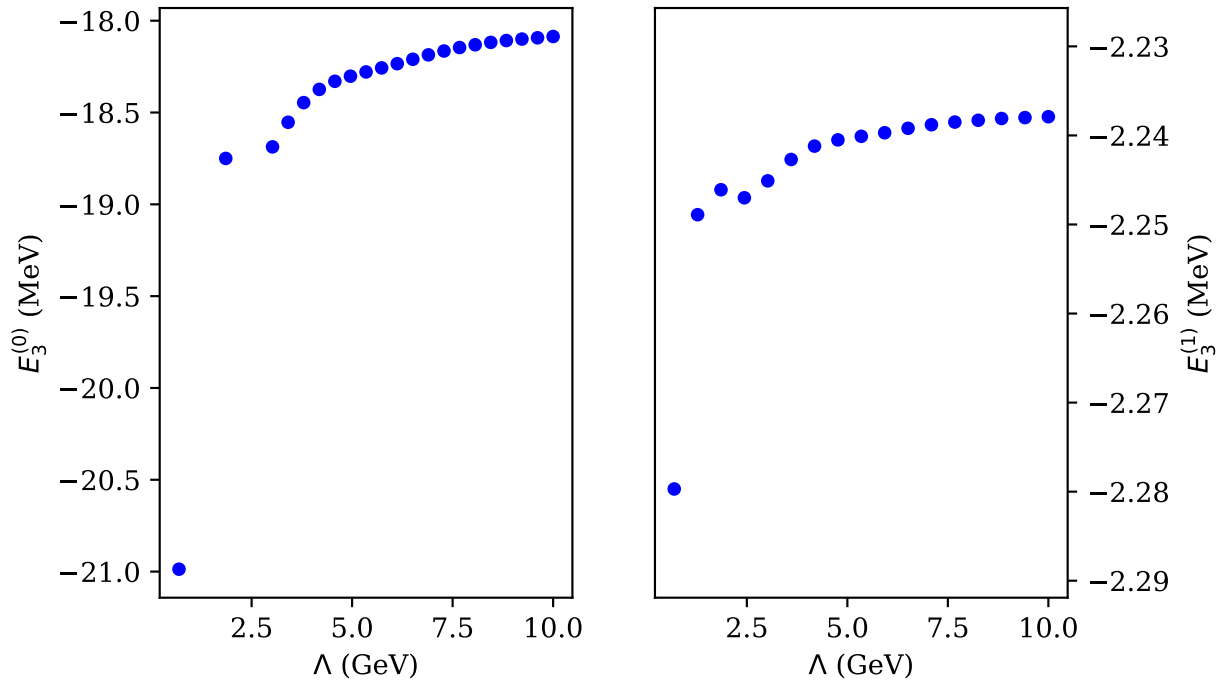


FIG. 10. [Left] Three-body ground state/resonance energy as a function of the short-distance cutoff. [Right] Three-body excited state/resonance energy as a function of the short-distance cutoff.

## IV. SUMMARY

In this manuscript, we have set out to understand the renormalization properties of the FRIC potential in the two- and three-body sector. In particular, we have studied the regulator dependence of observables such as two-body phase shifts, three-body binding energies, the atom-dimer scattering length, phase shifts, and inelasticity parameter. Motivated by a recent development in the nuclear theory community, we did these calculations using different, frequently used regulator functions.

Our results in the two-body sector confirm that the two-body sector is properly renormalized. One input parameter is required (at leading order) to renormalize one low-energy counterterm and thereby the two-body sector. In the three-body sector, we have demonstrated that a three-body force is not needed at leading order to renormalize three-body observables for the inverse cube interaction.

In both the two- and three-body sectors, we have observed significant oscillatory behavior in the cutoff dependence of observables. These oscillations are not captured by a simple

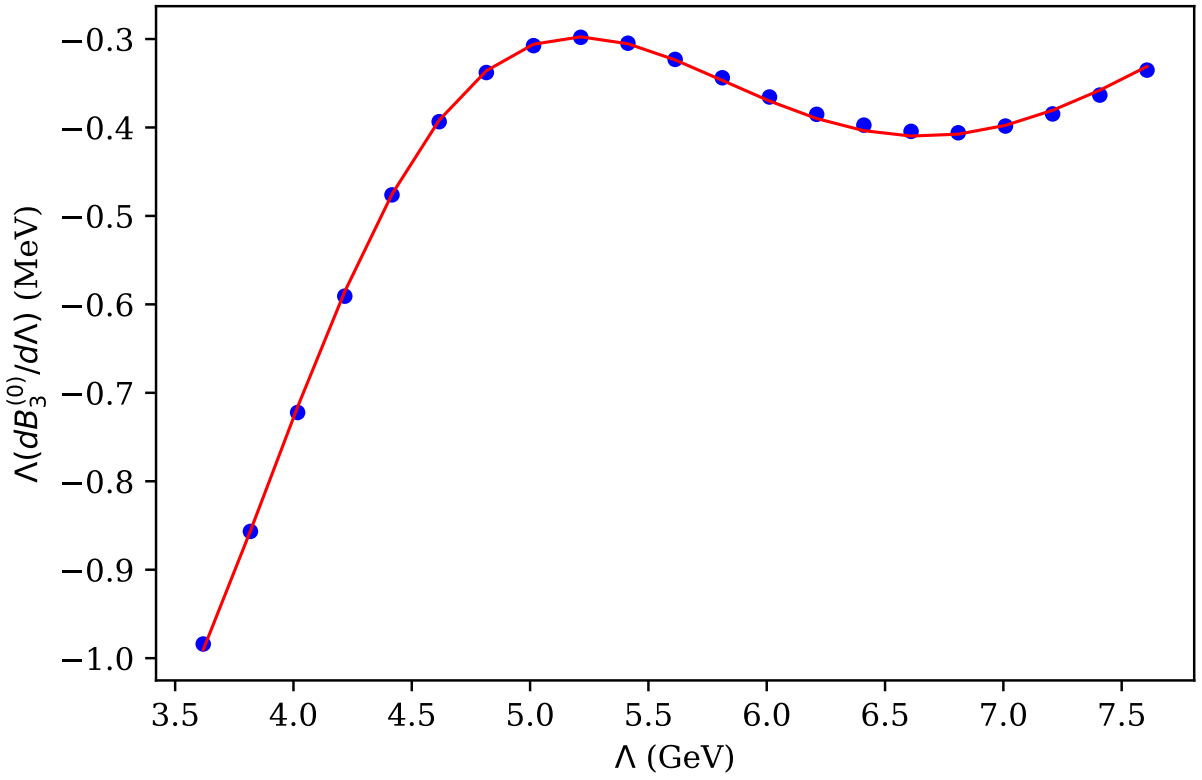


FIG. 11. RG analysis of the three-body, ground-state binding energy. The blue circles are the calculation. The red line represents a fit to Eq. (40) with $n_{\rm min} = 1.4$ and the values of $h$ and $f$ taken from the same fit of the atom-dimer scattering length.

power series expansion.

Instead, we have empirically found that a generalized oscillatory dependence of the form presented in Eq. (40) allows accurate fits of the data to be made and a much clearer picture of the power of the cutoff dependence to be revealed.

Our analysis strongly indicates that $n$ is smaller in the three-body sector than in the two-body sector. This would suggest that a three-body force is needed at next-to-leading order.

Our analysis also indicates that $n$ is consistent with approximately 1.5 for two-body observables and approximately 1 for three-body observables. It is an interesting question whether this has any significance for the counting of two- and three-body counterterms in an EFT for the inverse cube potential. For example, the singular $1/r^2$ has been considered previously as the starting point for an EFT expansion in Ref. [21], however the inverse cube

| Observable | $n_{\min}$ | $\Lambda_{\text{lower}}$ (GeV) | $\Lambda_{\text{upper}}$ (GeV) | h ($\text{MeV}^{-1/3}$) |
|---|---|---|---|---|
| $a(\Lambda)$ | 1.7 | 3.6 | 10.0 | 1.5 |
| $\delta(\Lambda; E = 12\text{MeV})$ | 1.7 | 2.6 | 10.0 | 1.5 |
| $\sigma(\Lambda; E = 12\text{MeV})$ | 1.7 | 2.4 | 10.0 | 1.5 |
| $\delta(k)$ | 1.5 | 3.4 | 6.7 | — |
| $a_{AD}(\Lambda)$ | 1.3 | 3.1 | 8.1 | 1.5 |
| $\delta_{2+1}(\Lambda; E = 10\text{MeV})$ | 1.3 | 3.7 | 7.7 | 1.4 |
| $\delta_{2+1}(\Lambda; E = 50\text{MeV})$ | 1.2 | 3.7 | 7.0 | 1.4 |
| $\eta_{2+1}(\Lambda; E = 50\text{MeV})$ | 1.3 | 3.7 | 7.0 | 1.5 |
| $\eta_{2+1}(\Lambda; E = 100\text{MeV})$ | 1.1 | 3.7 | 7.1 | 1.4 |
| $E_3^{(0)}$ | 1.4 | 3.5 | 7.8 | 1.5* |

TABLE I. $n_{\min}$ values for various two- and three-body observables alongside the bounds of cutoffs over which the fit to Eq. (40) was performed as well as the frequency that optimizes the fit. * The $h$ value for $E_3^{(0)}$ was taken from the fit of $a_{AD}$.

and all other singular coordinate space potentials need their own independent analysis.

Having tested several different local, semi-local, and nonlocal regulators and having found no significant differences above ≈2 GeV, we conclude that these oscillations are most likely attributable to the singular nature of the inverse cube potential in coordinate space.

In the future, we plan to carry out an analysis of higher order corrections in the three-boson and three-nucleon sector. However, we plan to also extend our work to the infinite range inverse cube potential that is of relevance to the atomic dipole interaction. This will let us combine the results obtained by Müller [11] with three-body observables and study the dependence of three-body observables on the boundary condition employed in the two-body sector. A more detailed analysis of the short-distance behaviour of the three-nucleon wave function might also provide novel insights into the power counting of electroweak currents [22].

## Appendix A: Local Regulator Sensitivity

To regulate the interaction

$$V_S(r) = -C_3 \frac{e^{-m_\pi r}}{r^3} \ , \tag{A1}$$

a general (local) regulator, $\rho(r; R)$, can be used such that the limit

$$\lim_{r\to 0} \rho(r; R) V_S(r) \ , \tag{A2}$$

is finite. We use regulators of the form

$$\rho(r; R) = (1 - e^{-(r/R)^{n_1}})^{n_2} \ , \tag{A3}$$

whose small $r$ behavior goes like $r^{n_1 n_2}$. As long as $n_1 n_2 \geq 3$, the regulator sufficiently meets the requirement of Eq. A2. However, our earliest calculations using the semi-local regulation scheme with $n_1 = 3$ and $n_2 = 1$ gave inconsistent results. Specifically, we observed unexpected cutoff dependence in the phase shifts as shown in Fig. 12. Simply increasing $n_2$ to 4 such that $n_1 n_2 = 4 > 3$ removes the dramatic changes in the phase shift. We have also compared our local regulators with those used by others [14, 23]. In the interest of consistency and to ensure we avoid unexpected cutoff dependence, we have used a local regulator of the form $n_1 = 2$ and $n_2 = 4$ for the calculations carried out it in this work. The unexpected cutoff dependence was observed exclusively when using semi-local regulation and only when $n_1 n_2 = 3$.

## ACKNOWLEDGMENTS

This work has been supported by the National Science Foundation under Grant No. PHY-1555030, and by the Office of Nuclear Physics, U.S. Department of Energy under Contract No. DE-AC05-00OR22725. A.D. acknowledges the support by the Alexander von Humboldt Foundation under Grant No. LTU-1185721-HFST-E.

---

[1] E. Epelbaum, H.W. Hammer, U.G. Meißner, Rev. Mod. Phys. **81**, 1773 (2009). doi: 10.1103/RevModPhys.81.1773. URL https://link.aps.org/doi/10.1103/RevModPhys.81.1773

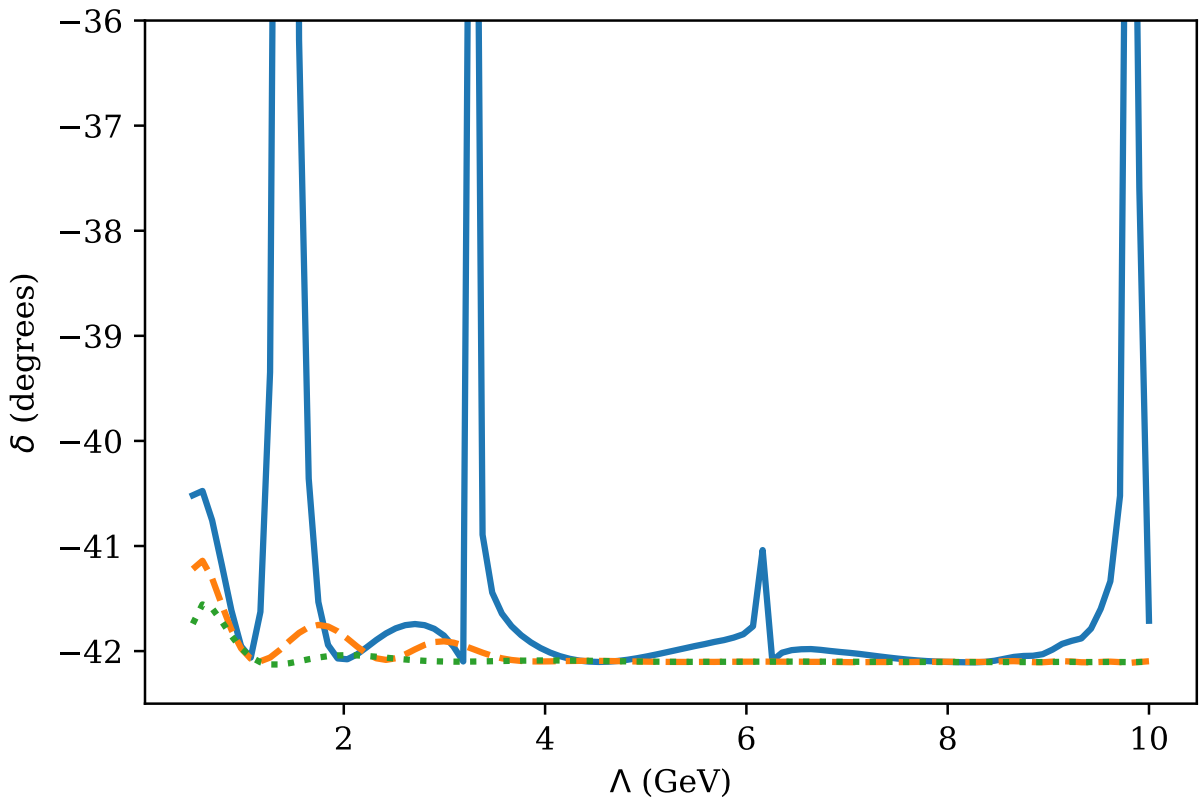


FIG. 12. Phase shifts at a center-of-mass energy of 1 MeV for three different regulators. Per Eq. (A3), the solid, blue line corresponds to $n_1 = 3$ and $n_2 = 1$. The dashed, yellow line corresponds to $n_1 = 4$ and $n_2 = 1$. The dotted, green line corresponds to $n_1 = 2$ and $n_2 = 4$.

[2] H.W. Hammer, A. Nogga, A. Schwenk, Rev. Mod. Phys. **85**, 197 (2013). doi: 10.1103/RevModPhys.85.197

[3] D.W.L. Sprung, W. van Dijk, E. Wang, D.C. Zheng, P. Sarriguren, J. Martorell, Phys. Rev. C **49**, 2942 (1994). doi:10.1103/PhysRevC.49.2942. URL https://link.aps.org/doi/10.1103/PhysRevC.49.2942

[4] M. Pavon Valderrama, E. Ruiz Arriola, Phys. Rev. **C72**, 054002 (2005). doi: 10.1103/PhysRevC.72.054002

[5] M. Pavon Valderrama, E. Ruiz Arriola, Phys. Rev. **C70**, 044006 (2004). doi: 10.1103/PhysRevC.70.044006

[6] A. Nogga, R.G.E. Timmermans, U.v. Kolck, Phys. Rev. C **72**, 054006 (2005). doi: 10.1103/PhysRevC.72.054006. URL https://link.aps.org/doi/10.1103/PhysRevC.72.054006

[7] M.C. Birse, Phys. Rev. C **74**, 014003 (2006). doi:10.1103/PhysRevC.74.014003. URL https://link.aps.org/doi/10.1103/PhysRevC.74.014003

[8] B. Long, C.J. Yang, Phys. Rev. **C85**, 034002 (2012). doi:10.1103/PhysRevC.85.034002

[9] Y.H. Song, R. Lazauskas, U. van Kolck, Phys. Rev. **C96**(2), 024002 (2017). doi:10.1103/PhysRevC.96.024002

[10] H.W. Grießhammer, PoS **CD15**, 104 (2016). doi:10.22323/1.253.0104

[11] T.O. Müller, Phys. Rev. Lett. **110**, 260401 (2013). doi:10.1103/PhysRevLett.110.260401. URL https://link.aps.org/doi/10.1103/PhysRevLett.110.260401

[12] B. Gao, Phys. Rev. A **59**, 2778 (1999). doi:10.1103/PhysRevA.59.2778. URL https://link.aps.org/doi/10.1103/PhysRevA.59.2778

[13] A. Gezerlis, I. Tews, E. Epelbaum, S. Gandolfi, K. Hebeler, A. Nogga, A. Schwenk, Phys. Rev. Lett. **111**(3), 032501 (2013). doi:10.1103/PhysRevLett.111.032501

[14] E. Epelbaum, H. Krebs, U.G. Meißner, The European Physical Journal A **51**(5), 53 (2015). doi:10.1140/epja/i2015-15053-8. URL https://doi.org/10.1140/epja/i2015-15053-8

[15] A. Roggero, A. Mukherjee, F. Pederiva, J. Phys. Conf. Ser. **527**, 012003 (2014). doi:10.1088/1742-6596/527/1/012003

[16] J.E. Lynn, K.E. Schmidt, Phys. Rev. C **86**, 014324 (2012). doi:10.1103/PhysRevC.86.014324. URL https://link.aps.org/doi/10.1103/PhysRevC.86.014324

[17] W. Frank, D.J. Land, R.M. Spector, Rev. Mod. Phys. **43**, 36 (1971). doi:10.1103/RevModPhys.43.36

[18] S.R. Beane, P.F. Bedaque, L. Childress, A. Kryjevski, J. McGuire, U. van Kolck, Phys. Rev. A **64**, 042103 (2001). doi:10.1103/PhysRevA.64.042103. URL https://link.aps.org/doi/10.1103/PhysRevA.64.042103

[19] W. Glöckle, The Quantum Mechanical Few-Body Problem. Texts and Monographs in Physics (Springer, Berlin, 1983). doi:10.1007/978-3-642-82081-6. URL https://link.springer.com/book/10.1007%2F978-3-642-82081-6

[20] W. Gloeckle, H. Witala, D. Huber, H. Kamada, J. Golak, Phys. Rept. **274**, 107 (1996). doi:10.1016/0370-1573(95)00085-2

[21] B. Long, U. van Kolck, Annals Phys. **323**, 1304 (2008). doi:10.1016/j.aop.2008.01.003

[22] M. Pavón Valderrama, D.R. Phillips, Phys. Rev. Lett. **114**(8), 082502 (2015). doi:10.1103/PhysRevLett.114.082502

[23] S. Binder, et al., Phys. Rev. **C98**(1), 014002 (2018). doi:10.1103/PhysRevC.98.014002